Transport and noise properties of YBCO nanowire based nanoSQUIDs

E. Trabaldo[1], R. Arpaia[1,2], M. Arzeo[1,†], E. Andersson[1], D. Golubev[3], F. Lombardi[1], T. Bauch[1]

[1] Quantum Device Physics Laboratory, Department of Microtechnology and Nanoscience, Chalmers University of Technology, SE-41296 Göteborg, Sweden
[2] Dipartimento di Fisica, Politecnico di Milano, Piazza Leonardo da Vinci 32, I-20133 Milano, Italy
[3] Low Temperature Laboratory (OVLL), Aalto University School of Science, P.O. Box 13500, 00076 Aalto, Finland
† Present address: European Organization for Nuclear Research, CERN, 1211 Geneva 23, Switzerland

E-mail: `thilo.bauch@chalmers.se`

February 2019

Abstract. The development of quantum limited magnetic flux sensors has recently gained a lot of attention for the possibility of detecting the magnetic moment of nanoscaled systems. Here, the ultimate goal is the observation of a single spin. Such sensors are of fundamental importance for applications, ranging from spintronics and spin-based quantum information processing, to fundamental studies of nano-magnetism in molecules and magnetic nanoclusters. A nano-scale Superconducting QUantum Interference Device (nanoSQUID) is indeed a promising candidate to reach this ambitious goal. Nanowires, fabricated of High critical Temperature Superconductors (HTS), have been shown to be a valid candidate for the realization of nanoSQUIDs. A crucial requirement to achieve the necessary flux sensitivity and spatial resolution, is a SQUID loop on the nanometer scale. Moreover, HTS nanowire-based SQUIDs in combination with large area pickup loops or flux transformers might become instrumental in magnetometer applications, such as magneto encephalography and low field magnetic resonance imaging, where low intrinsic magnetic field noise is required. In this review we will give a survey on the state of the art of $YBa_2Cu_3O_{7-\delta}$ thin film nanowires and their implementation in low noise nanoSQUIDs and magnetometers.

Contents

1. Introduction

During the recent years a lot of effort has been invested to develope nano-scale Superconducting QUantum Interference Devices (nanoSQUIDs) implementing superconducting nanowires in Dayem bridge or variable thickness junction configurations [1, 2, 3, 4, 5] with the goal to detect the magnetic moment of nanoscale systems [6, 7, 8, 9, 10, 11, 12].

A SQUID loop on the nanometer scale is indeed a crucial requirement for the detection of a single atomic spin, a holy grail in fundamental measurement techniques [10]. At the moment, the realization of such nanoSQUIDs is well established for Low critical Temperature Superconductors (LTS), e.g. Nb, [13, 14, 7]. NanoSQUIDs made of cuprate High critical Temperature Superconductors (HTS) might extend the operational temperature (from mK to above 77 K) and the range of magnetic fields that can be applied to manipulate spins compared to LTS based nanoSQUIDs.

Moreover, HTS nanowire-based SQUIDs, in combination with large area pickup loops or flux transformers, might become instrumental in magnetometer applications, such as magneto encephalography and low field magnetic resonance imaging, where low intrinsic magnetic field noise is required [15, 16].

The aim of this review is to give a short overview on the development of HTS nanowire based SQUIDs over the past few decades. For reviews on macroscopic HTS weak links and SQUIDs implementing conventional junctions such as grain boundaries, step edges, and ramp junctions see Refs. [17, 18, 19]. A review on nanoSQUIDs including also YBCO grain boundary based devices is given in Ref. [20]. An exhaustive review on LTS based nanoSQUIDs is given in Ref. [12].

NanoSQUIDs based on nano-bridges have been at the forefront of research on quantum-limited devices since their first introduction in 1980, by Voss et al. [21]. These first LTS based nanoSQUIDs were based on Nb nanowires and demonstrated the lowest intrinsic energy resolution at the time. While the fabrication of LTS nanoscale weak-links can be achieved with standard fabrication techniques, the main difficulty in the realization of nanoscale cuprate HTS devices is their chemical instability (mainly oxygen out-diffusion). This, combined with cuprate's extreme sensitivity to disorder, due to their small superconducting coherence length ($\sim$ 2 nm in the CuO_2 a-b planes), makes the realization of high-quality HTS nanoscale weak-links a very challenging task. As a result, $YBa_2Cu_3O_{7-\delta}$ (YBCO) nanobridges were not realized until 1993. During the first half of the 1990's, various groups [22, 23, 24, 25] reported on the fabrication and characterization of sub-micron YBCO structures with Josephson-like properties at temperatures above 77 K. However, the superconducting properties of these YBCO nano-structures were strongly suppressed compared to the bare film properties. For instance, the critical current of these YBCO nanobridges did not scale linearly with the width of the bridges. This can be interpreted as a deterioration of the YBCO nano-structure during the fabrication process.

In 1994, Schneider et al. reported on the first nanobridge-based dc SQUID

patterned from YBCO thin films [26]. These devices exhibited voltage modulations as a function of the external magnetic field up to 85 K. However, they didn't show the expected modulation of the critical current. Furthermore, the large values of magnetic flux noise strongly limited the possible technological application of these devices, e.g. as magnetometers. Nevertheless, these first results opened the way to extensive effort for the realization of HTS nanowire based nanoSQUIDs.

Soon after the development of the first nanowire based SQUIDs, Pedyash et al. reported a study on the transport properties of these devices [27]. From the observed SQUID voltage modulations as a function of temperature T, the authors concluded that the weak-links behaved like superconductor-normal conductor-superconductor (SNS) junctions at temperatures close to the superconducting transition temperature T_C of the electrodes. At low temperature the weak-links behaved instead as SS'S junctions, where S' represents the superconducting weak link with a T_C lower than the one of the electrodes. This behavior is again an indication that the patterning procedure seriously degraded the superconducting properties of the nanobridges.

The main breakthrough in YBCO nanowire fabrication was reported in 2013 [28, 29]. Recent advances in nanopatterning techniques applied to HTS thin films have made possible the realization of YBCO nanowires with cross sections down to $50 \times 50\,\mathrm{nm}^2$ [28, 29, 30, 31]. The critical supercurrents achieved in such nanowires are close to the theoretical depairing limit demonstrating the pristine properties of the nanostructures [29].

NanoSQUIDs based on Au capped YBCO nanowires have shown SQUID-like modulations of the critical current with an externally applied magnetic field in the temperature range slightly below the critical temperature down to 300 mK [4]. Here white flux noise levels below 1 $\mu\Phi_0\mathrm{Hz}^{-1/2}$ have been achieved at $T = 8$ K. Additional improvements in the fabrication process using thinner YBCO films (down to 10 nm) without the use of a Au capping layer have further increased the flux sensitivity resulting in white noise values below 500 $\mathrm{n}\Phi_0\mathrm{Hz}^{-1/2}$ at T = 18 K in YBCO nanowire based nanoSQUIDs [32].

First attempts of realizing a magnetometer coupling galvanically a large area pickup loop to a nanoSQUID resulted in increased effective areas with magnetic flux noise still below 1 $\mu\Phi_0\mathrm{Hz}^{-1/2}$ [15]. This makes such devices very attractive for applications requiring magnetic field sensitivities in the $\mathrm{fTHz}^{-1/2}$ range.

2. Theoretical Modeling of HTS nanowires

In this section we will give a short overview on a macroscopic model based on the Ginzburg Landau (GL) theory for the description of the electronic transport in superconducting nanowires. From this simple model the main transport properties, such as the depairing critical current and the current phase relation (CPR) of superconducting nanowires (for various length and width regimes), can be derived. Although the GL theory is, strictly speaking, only valid at temperatures close to the

superconducting transition temperatures, expressions such as the current phase relation for long superconducting wires can still be reasonably well approximated by the GL expression at temperatures well below the superconducting transition temperature [33].

2.1. Current Phase Relation of HTS nanowires

2.1.1. Ginzburg Landau equations The Ginzburg Landau (GL) theory describes phase transitions of materials in terms of their free energy. A phase transition is an abrupt change in one or more physical properties of a material as a function of a thermodynamical variable like temperature, T, and can be described in terms of the free energy density, $\tilde{F}$, of the system. Since superconductivity is a second order phase transition, the discontinuity occurs only in the second derivative of the free energy of the system.

Ginzburg and Landau expanded upon the London theory [34] and generalized the local electrodynamics in superconductors developing an expression for the free energy density of a superconductor close to the superconducting transition temperature T_C. The GL theory introduces the following properties: i) A spatial variations of the condensate density $n_P(\vec{r})$; ii) A magnetic self-energy term in the free energy expression, which takes into account variations of $n_P(\vec{r})$ due to the field.

By introducing a complex order parameter

$$\Psi(\vec{r}) = |\Psi(\vec{r})|\, e^{i\phi(\vec{r})} \tag{1}$$

where $n_p = |\Psi(\vec{r})|^2$ and $\phi(\vec{r})$ is the phase as a function of position, one can obtain the expression for the free energy, F, for small variations of Ψ and $\vec{\nabla}\Psi$ around T_C as

$$F = F_n + \int_V dV [\alpha\Psi^*\Psi + \frac{1}{2}\beta(\Psi^*\Psi)^2 + \frac{1}{4m}|i\hbar\vec{\nabla}\Psi - 2e\bar{A}\Psi|^2] + \int \frac{\mu_0}{2}|\vec{M}|^2 dV, \tag{2}$$

where F_n is the normal state energy and $\vec{M}$ the magnetization.

Minimizing this equation with respect to variations in Ψ and Ψ^* results in the first GL equation

$$\alpha\Psi + \beta\,|\Psi|^2\,\Psi + \frac{1}{4m}\left(-i\hbar\vec{\nabla} + 2e\vec{A}\right)^2\Psi = 0. \tag{3}$$

with the boundary condition

$$\nabla_n\Psi - \frac{2e}{i\hbar}A_n\Psi = 0, \tag{4}$$

where $e \simeq 1.6 \times 10^{-19}$ C is the elementary charge, m the electron mass, and $\vec{A}$ the vector potential. The suffix n refers to the component normal to the superconductor surface. For temperatures close to T_C the term α can be approximated by $\alpha \propto (T - T_C)$ and β can be treated as a positive constant. Similarly, minimizing the GL free energy F with respect to variations of the vector potential $\vec{A}$ results in the second GL equation

$$\vec{J}_s = \frac{i\hbar e}{2m}\left(\Psi^*\vec{\nabla}\Psi - \Psi\vec{\nabla}\Psi^*\right) - \frac{2e^2}{m}\vec{A}|\Psi|^2, \tag{5}$$

with $\vec{J}_s$ the supercurrent density. From the GL equations (Eqs. 3,5) one can derive two characteristic lengths scales, first the coherence length $\xi = \sqrt{\hbar^2/4m|\alpha|}$, which describes the length scale over which the order parameter can vary. Second, the London penetration depth $\lambda = \sqrt{m/2\mu_0 e^2 n_{P,0}} = \sqrt{m\beta/2\mu_0 e^2|\alpha|}$, which is the length scale over which the supercurrent density can vary. Inserting the expression for the pair condensate wave function (Eq.1) into the second GL equation (Eq.5) one obtains

$$\mu_0\lambda^2\vec{J}_s = -\frac{|\Psi(\vec{r})|^2}{n_{P,0}}\left(\frac{\hbar}{2e}\vec{\nabla}\phi + \vec{A}\right), \tag{6}$$

which relates the supercurrent density to the phase gradient, $\vec{\nabla}\phi$, and the vector potential, $\vec{A}$.

If a thin insulating barrier is sandwiched between two superconducting electrodes, tunneling of superconducting charge carriers can arise due to a phase difference between the electrodes. In this scenario, the two superconducting electrodes are coupled through the barrier forming a so-called Josephson Junction (JJ) [35]. A similar effect as for JJs is observed in systems which do not strictly have barriers, but are instead characterized by a local discontinuity of the order parameter, e.g. nanowires and weak links.

2.1.2. Short one-dimensional S/S'/S weak links The existence of the Josephson behavior in superconducting narrow bridges was predicted in the 1960's [36], right after the discovery of the Josephson effect between two superconductors separated by a thin insulating barrier. Aslamazov and Larkin considered two bulk superconducting electrodes separated by a short ($l \ll \xi$) one-dimensional ($w,t \ll \xi$) link of the same material, where l,w and t are the length, width and thickness of the weak link, respectively (see Fig.1). In this limit, one can write the GL equation for the current
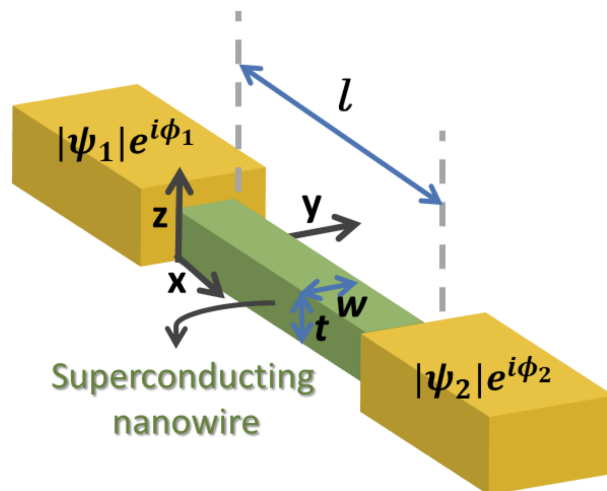

Figure 1. Schematic of a Superconductor-Superconducting narrow bridge-Superconductor (S-S'-S) weak link.

density as a function of phase difference $\varphi = \psi_1 - \psi_2$ between the two electrodes [37]

$$j_s^{AL} = \frac{e\hbar|\Psi_\infty|^2}{ml}\sin\varphi = \frac{\Phi_0}{2\pi\mu_0\lambda^2 l}\sin\varphi, \tag{7}$$

with $|\Psi_\infty|^2 = n_P$ the equilibrium pair density in the electrodes. This equation is very general; it does not depend on the electronic mean free path, ℓ, in the weak link, i.e. it is valid for both dirty ($\ell < \xi$) and clean ($\ell > \xi$) superconductors. Therefore it is applicable to all types of weak links close to T_c. According to Eq.7, near T_c the current phase relation is always sinusoidal, independent of the material of the weak link.

2.1.3. Long one-dimensional S/S'/S weak links Likharev and Yakobson considered the effect of an increasing weak link length on the Current Phase Relation (CPR) for temperatures close to T_C. In their model the current phase relation evolves from a sinusoidal to a 'slanted' sinusoidal and eventually to a multivalued CPR for increasing length of the bridge (for $l > 3.49\xi$). In the multivalued current phase relation (see Fig. 2) the unstable (lower reverse) branch corresponds to a local sharp drop of the order parameter (pair density) in the center of the nanowire, i.e. to the nucleation of phase slip centers. For wires of length $l > 10\xi$ the maximum current value in the respective current phase relation saturates at a value given by the depairing current density. The value of the depairing current density will be derived later in this section. Only short weak links with $l < 3.49\xi$ that have a single valued current phase relation can be considered to feature an 'ideal' Josephson effect, while the properties of long weak links with $l > 3.49\xi$, which are characterized by a multivalued current phase relation, are determined by depairing effects.
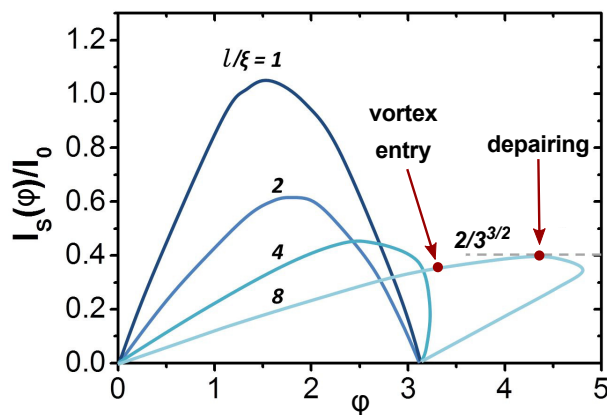
Figure 2. Current phase relation for various lengths of a weak link of the type S/S'/S slightly below T_c. The currents are normalized to the value $I_0 = \Phi_0/2\pi\mu_0\lambda^2\xi$. Only the positive current branch is shown. Adapted from Likharev and Yakobson [38].

In the limit of long ($l \gg \xi$) and one-dimensional ($w, t \ll \xi$ and $wt \ll \lambda^2$) wires one can easily derive the stable branch of the current phase relation from the GL equations. The condition $w, t \ll \xi$ ensures that the modulus of the wave function stays constant

across the cross section of the wire. The property $wt \ll \lambda^2$ results in a homogeneous current distribution inside the wire. Moreover in this limit the kinetic energy of the Cooper pair flow dominates over the magnetic energy produced by the same current flow by roughly a factor λ^2/wt (see discussion below). Therefore, in this regime we can neglect the magnetic self-field terms in the GL model. Assuming that the nonlinear effects occur only in the wire and considering that the modulus of the wave function stays constant along the wire one obtains from the first GL equation (Eq.3) and Eq.6

$$\vec{J}_{\text{s}} = \frac{\Phi_0}{2\pi\mu_0\xi\lambda^2} \left(\frac{\varphi\xi}{l} - \left(\frac{\varphi\xi}{l} \right)^3 \right). \tag{8}$$

This equation is maximized ($d\vec{J}_{\text{s}}/d(\varphi/l) = 0$) at a phase gradient $\varphi_{\text{d}}/l = 1/\sqrt{3}\xi$. This correspond to the depairing critical current density, which can be written as

$$J_{\text{d}} = \frac{\Phi_0}{3\sqrt{3}\pi\mu_0\lambda^2\xi} \tag{9}$$

Using Eq.8 we can now write the CPR of a long nanowire with cross sectional area wt

$$I_{\text{s}} = \frac{\Phi_0}{2\pi L_{\text{k}}} \left(\varphi - \left(\frac{\xi}{l} \right)^2 \varphi^3 \right), \tag{10}$$

where the kinetic inductance of the wire, L_k, is given by

$$L_{\text{k}} = \mu_0\lambda^2 \frac{l}{wt}. \tag{11}$$

Comparing the kinetic inductance to the geometric inductance of a wire, which is related to the magnetic field generated by the transport current and approximately given by $L_{\text{g}} \simeq \mu_0 l$, we see that for narrow enough nanowires ($wt < \lambda^2$) the kinetic inductance dominates the total inductance of a nanowire. It is important to note that this kind of current phase relation is defined over a much wider phase difference range compared to an 'ideal' Josephson junction for which the current phase relation is fully described in a phase difference interval $-\pi < \varphi < \pi$. Indeed, for a long nanowire ($l \gg \xi$) the current phase relation is defined in a range $-l/\sqrt{3}\xi < \varphi < l/\sqrt{3}\xi$, which for $l \gg \xi$ can be much larger than 2π. For bias currents much smaller than the depairing critical current, $I_{\text{d}} = J_{\text{d}}wt$, the phase difference is very small. This together with the small prefactor in the cubic term in Eq.10 allows to truncate the expression of the current density to the first order term. The nanowire behaves therefore like a linear inductor, with value given by the kinetic inductance, where the phase difference between the two ends grows linearly with bias current. Only for bias currents close to the depairing limit the cubic term in the current phase relation makes the wire behave like a nonlinear inductor.

Once the depairing critical current is reached, phase slip centers nucleate inside the wire. The phase slip must be 2π or integer multiples of it because the order parameter in the macroscopic leads is defined modulo 2π. Moreover, since the supercurrent density

must stay constant, we can derive from Eq.6 (neglecting once more the vector potential) a constraint on possible variations of the wave function

$$|\Psi(x)|^2 \frac{d\varphi}{dx} = \text{const} \propto I. \tag{12}$$

Langer and Ambegaokar used this constraint to argue that one could have $|\Psi| \rightarrow 0$ just so long as the phase varied rapidly in space [39]. As the order parameter reaches zero at some point along the 1D wire, the phase changes by 2π in a process known as a phase slip. This phase slip process can be also depicted in the current phase relation shown in Fig. 3. When increasing continuously the phase difference between the two ends of the wire, by e.g. applying a constant voltage, the current through the wire eventually reaches the depairing critical current. At this point a phase slip occurs and the phase changes by 2π. Here, the supercurrent in the nanowire is given by the current phase relation evaluated at $\varphi_d - 2\pi$. This behavior can be also mimicked by periodically repeating the current phase relation modulo 2π (see Fig.3(b)). In this representation the phase slip is equivalent to jumping vertically to the adjacent stable branch.
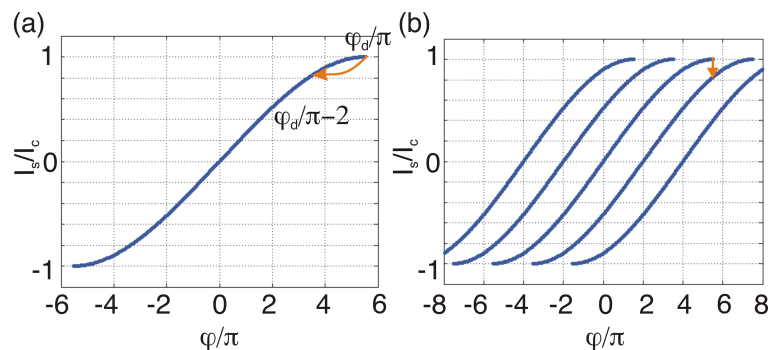
Figure 3. a) Current phase relation of a superconducting nanowire of length $l = 30\xi$ (only stable branch shown). The orange arrow indicates a phase slip process when the critical current I_c is reached, reducing the phase difference by 2π. (b) 2π-periodic representation of the current phase relation shown in (a). Here a phase slip occurring at I_c corresponds to a vertical jump to the neighboring stable branch.

Up to now only one-dimensional wires were considered. However, the HTS nanobridges reported in literature have lateral dimensions larger than the coherence length ($\xi_0 \simeq 2$ nm for YBCO). Still many of the above results are applicable for structures wider than the coherence length.

2.1.4. Long S/S'/S weak links for increasing wire width According to Likharev [41], an ideal Josephson behavior is expected for very short superconducting structures with $l \leq 3.49\xi$. Structures belonging to this dimensional regime, due to short length scales, do not allow any instabilities to develop along their length and show a single value current phase relation. In Fig.4, this regime lies below the dashed line (region I) which defines a critical length scale ($l_c \simeq 3.49\xi$) for the short structures to show an ideal Josephson behavior. Such a regime has been exhaustively explored in LTS materials
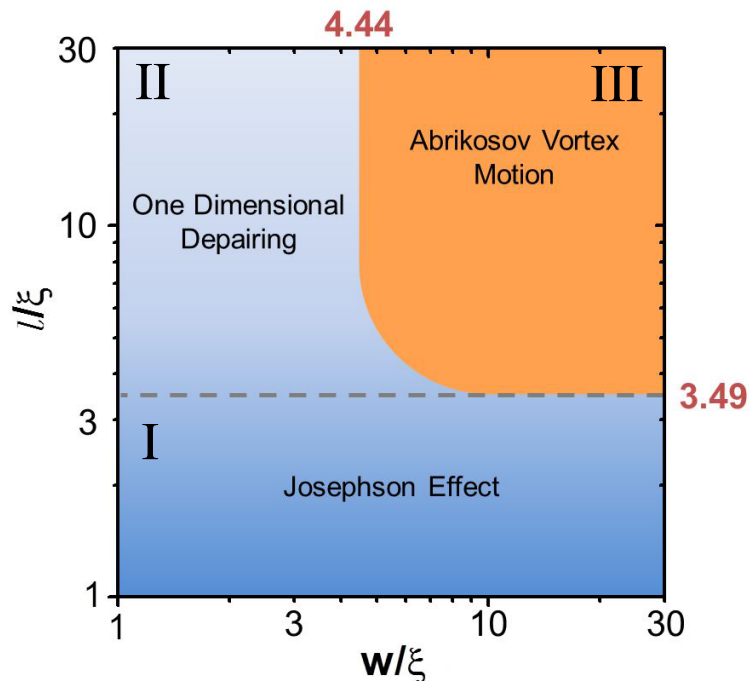
Figure 4. Likharev criteria for the origin of the current phase relation for different S/S'/S weak link dimensions. Region I corresponds to short nanowires and is representative of an ideal Josephson behavior. Region II represents the dimensional regime where the one dimensional depairing limit is valid i.e $w < 4.44\xi$. In region III (long $l > 3.49\xi$ and wide $w > 4.44\xi$ wires) Abrikosov vortex motion starts playing a role. Adapted from Likharev [40].

[3], whereas, due to much shorter coherence length, this has not been possible for HTS. The CPR of S/S'/S weak links with $l > 3.49\xi$ depends on the width of the structures, and, as sketched in Fig.4, two regimes can be distinguished:

Region II - $w < 4.44\xi$ the current phase relation is the result of one-dimensional depairing as we discussed in the previous section.

Region III - $w > 4.44\xi$ Abrikosov vortices may enter these structures. In the case of bridges with $t < \lambda$ and $w < \lambda_P$, where $\lambda_P = \lambda^2/t$ is the Pearl length, the current density can be assumed homogeneous. Therefore, the 3-dimensional GL equations can, to a good approximation, be reduced to a 1-dimensional form [42, 43]. The problem of a current carrying nano-bridge of this type in zero externally applied magnetic field has a similar solution for the current phase relation as the one derived for the pure 1-dimensional case (Eq.8) [43]. Thence, in this limit the current phase relation might be still approximated by the multi-valued current phase relation depicted in Fig.2 [44]. However, it is important to point out that the maximum critical current density in this case is not given by depairing effects, i.e. phase slips, instead the critical current density will be limited by Abrikosov vortex entry into the nano-bridge, as we will discuss below.

The critical current density at which vortices nucleate and enter the superconducting bridge can be estimated by considering the bias current dependence of the vortex

entry edge barrier. For bias currents smaller than the critical current, a finite edge barrier prevents vortices from entering the wire [45]. This edge barrier, the so called Bean-Livingston barrier, can be understood from the distortion of the circulating currents of a vortex sitting close to the wire edge, i.e. the normal component of the current at the edge has to be zero [45]. This current distortion can be modeled by an image vortex sitting outside the wire resulting in an attractive interaction of the vortex with its image vortex towards the edge of the wire. Increasing the bias current from zero to a finite value gradually reduces this edge barrier. For bias currents approaching the critical current, the barrier is eventually completely suppressed at a distance of the order of the coherence length from the wire edge, allowing vortices to enter the wire [45]. The resulting vortex motion across the wire, driven by the Lorentz force, causes a finite voltage drop along the wire.

According to Bulaevskii [43] the energy barrier for a vortex as a function of position in presence of a uniform bias current is given by

$$U(y, I_b) = \mu^2 \epsilon_0 \left[\ln\left(\frac{2w}{\pi\xi} \sin\frac{y\pi}{w} \right) - \frac{I_b}{\mu^2 I_0} \frac{y\pi}{w} \right], \tag{13}$$

with

$$\epsilon_0 = \frac{\Phi_0^2 t}{4\pi\mu_0\lambda^2} \tag{14}$$

the characteristic energy of a vortex in thin films and $I_0 = \Phi_0 t/4\mu_0\lambda^2$. The bias current dependent factor μ^2 describes the order parameter suppression by the bias current and is given by

$$\mu^2 = \frac{|\Psi|^2}{|\Psi_\infty|^2} = 1 - \left(\frac{\varphi\xi}{l} \right)^2. \tag{15}$$

According to Bulaevskii et al. [43] the critical phase gradient at which the barrier disappears in narrow nano-bridges with width $w < \lambda_P$ is

$$\frac{\varphi_v}{l} = \frac{1}{\xi\tilde{e}}, \tag{16}$$

with $\tilde{e} = 2.718$. Comparing the critical phase gradient for vortex entry with the critical phase gradient for depairing $(\varphi_d/l = 1/\sqrt{3}\xi)$, i.e. phase slip, one obtains

$$J_v = J_d \frac{(1/\tilde{e})(1 - (1/\tilde{e}^2))}{(1/\sqrt{3})(1 - (1/3))} \simeq 0.826 J_d. \tag{17}$$

This suggests that the critical current density J_v for vortex entry is slightly smaller than the depairing critical current density J_d (see Fig.3). Even for wide nano-bridges $(w > \lambda_P)$, where the current profile across the width is enhanced at the edges, it has been shown, by numerically solving the time-dependent GL equations [42], that as soon as the current density at the bridge edges reaches values close to the depairing value vortices may nucleate and enter the bridge structure.

2.2. Thermal Activation of Abrikosov Vortices

As discussed above in the case of long ($l \gg 3.49\ \xi$) and wide ($w \gg 4.44\ \xi$) superconducting bridges, vortex crossing from one edge of the bridge to the other, perpendicularly to the bias current, causes the transition from the superconducting state to the finite voltage state. Therefore, one can identify vortex entry and the subsequent vortex motion across the nano-bridge width as the dominant mechanism of dissipation [43]. In the following we analyze the role of thermally activated vortex dynamics on dissipation close to the superconducting transition temperature T_C in long and wide nanowires made of type II superconductors.

Starting from the vortex entry barrier (see eq.13), Bulaevskii et al. [43] derived the vortex crossing rate in the framework of the Langevin equations for viscous vortex motion. From the known solutions of the corresponding Fokker-Planck equations one can write for the zero bias resistance on a nanowire of length l [46]

$$R_{\mathrm{v}}(T) = 7.1 R_{\mathrm{S}} \frac{l\xi(T)}{w^2} \left(\frac{\mu^2}{k_{\mathrm{B}}T} \frac{\Phi_0^2 t}{4\pi\mu_0\lambda_{\mathrm{L}}^2(T)}\right)^{3/2} \exp\left(-\frac{\mu^2}{k_{\mathrm{B}}T} \frac{\Phi_0^2 t}{4\pi\mu_0\lambda_{\mathrm{L}}^2(T)} \ln\frac{1.47w}{\pi\xi(T)}\right) \quad (18)$$

where R_{S} is the sheet resistance of the wire, k_B is the Boltzmann constant, and μ^2 is equal to 1 in the zero bias limit. By fitting measured resistance vs temperature data of long and wide nanobridges to Eq.18 one obtains values of ξ, λ, and T_{C}, which allows to assess the quality of the nanobridges [46, 47, 48].

3. YBCO nanowire fabrication and characterization

The first sub-micron YBCO wires have been obtained by defining an etching mask on top of a YBCO film with Electron Beam Lithography (EBL) followed by sputter etching [23, 24] or a combination of Reactive Ion Ecthing followed by Ion Beam Etching (IBE) [22, 25]. In these early studies, the reported critical currents of the nanowires were lower than what was predicted by theory. The etching was identified as the critical step to maintain the pristine quality of the YBCO nanostructures. In the decade following these first fabrication studies, several alternative techniques have been introduced for obtaining YBCO nanowires.

One of the most prominent alternatives to IBE is to define nanostructures with Focused Ion Beam (FIB) milling [2, 49]. Here, the macroscale features of the device are usually predefined by physical or chemical etching. The FIB is used to define the smaller, nano-scale structures. FIB has the advantage of being more flexible than EBL followed by IBE. FIB has been used for the fabrication of nano-SQUIDs [2] and photon detectors [49]. FIB can also be used in conjunction with standard EBL and IBE to fabricate Josephson Junctions (JJ). This is achieved by introducing local damage in YBCO structures [50, 51]. This technique has been instrumental to define JJs, resulting in high quality SNS and SIS junctions [51, 52].

The ion milling process is responsible for most of the degradation of nanowires. Alternative fabrication techniques have been proposed to obtain YBCO nanostructures

without involving IBE or FIB. One of these alternative is to grow directly YBCO nanowires via a growth template. This avoids both mechanical and chemical etching, greatly reducing the damage to the nanostructures. Arrays of YBCO nanowires have been grown in porous alumina, reaching lengths of several μm [53]. SrTiO$_3$ films have also been used as template for the growth of submicron structures. Both amorphous [54] and porous [55] SrTiO$_3$ have been used to integrate nanostructures of YBCO in macroscale structures. These techniques have the advantage of reducing the structural damage, but present limited control over the position, dimensions and shape of the nanostructures. Moreover, while the resulting structures have been successfully integrated in devices, this requires additional fabrication steps, adding another layer of complexity to template fabrication techniques.

A different fabrication technique involves a nanowire pattern transfer via a special superlattice [56]. This technique allowed to fabricate YBCO structures with lateral size as small as 10 nm, with length in the μm scale. However, these narrow YBCO structures showed superconducting properties only at temperatures below 20 K. Another alternative technique involves using an Atomic Force Microscope (AFM), in contact mode. With this last technique, nanobridges with widths down to 500 nm have been reported [57].

In the last decade, the IBE-based nanopatterning procedures for cuprates have greatly improved resulting in high quality YBCO nanowires [29, 30]. The resulting nanostructures are characterized by critical current density approaching the depairing limit. The ultimate lateral dimensions have been reduced down to cross-sectional areas as small as 50×10 nm^2, retaining film-like qualities [32]. In the following section, the fabrication methods for the realization of high quality YBCO nanowire [29, 30] will be introduced and analyzed.

3.1. Nanopatterning of YBCO films

The realization of pristine superconducting nanostructures is of essential importance to enable fundamental studies of superconductivity at the nano scale and operational reproducible devices such as SQUIDs. The nanopatterning of cuprate HTS has been a longstanding challenge for many decades. This is mainly related to the chemical instability of these materials and the extreme sensitivity to defects and disorder due to the very short superconducting coherence length ξ (of the order of 2 nm).

The most viable technology for the realization of cuprate HTS nanostructures is the pattern transfer through a hard mask using Ar ion milling into a HTS thin film [58, 59, 60]. In the following we summarize the fabrication process described in Refs. [28, 29].

First, a 50 nm thick YBCO film is grown by Pulsed Laser Deposition (PLD) on a (110) MgO substrate. A 50 nm Au film is subsequently deposited on top of the YBCO acting as a protective layer for the YBCO film during the patterning process. In the third step, a 100 nm thick amorphous carbon film is grown by PLD over the Au layer.
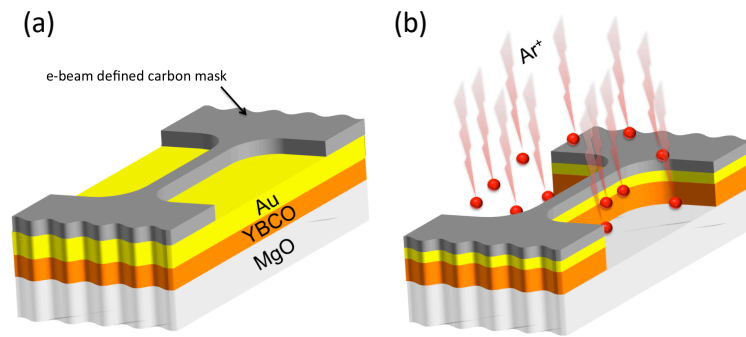
Figure 5. (a) Sketch of the amorphous carbon mask on top of a YBCO/Au bi-layer. (b) Sketch of the pattern transfer into the YBCO film through the carbon mask during the ion milling

The carbon film is first patterned by e-beam lithography and will then act as an ion milling mask for the pattern transfer into the YBCO film [58] (see Fig. 5). The ion milling process is indeed a crucial step for the realization of pristine nanostructures. An ion acceleration voltage close to a threshold value of $V \simeq 300$ V, below which YBCO is not etched, is used in order to minimize the damages to the nanostructures during the etching. A typical patterned YBCO nanowire is shown in Fig. 6.
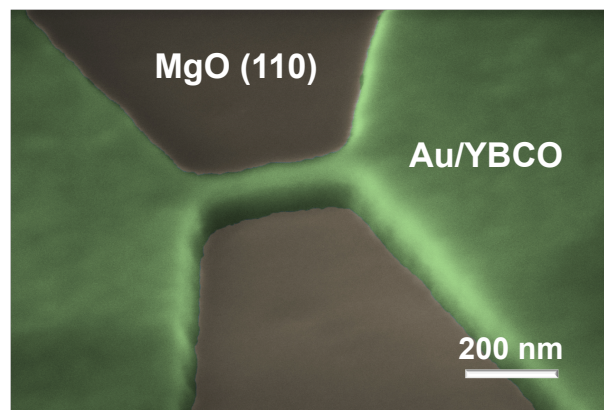
Figure 6. Scanning electron microscopy image of a 200 nm long YBCO nano wire.

3.2. Critical current of YBCO nanowires

As already pointed out in the previous section, HTS nanostructures may undergo a strong degradation during the patterning and, as a consequence, their superconducting properties would be seriously affected. To assess the homogeneity of the structures, a valuable test is the measurement of the critical current density $J_{\rm C}$ (defined as the ratio between the measured critical current and the wire cross section), which is very sensitive to any local non-uniformity and damage of the wire [61].

Theoretically, an infinite long wire with width smaller than the Pearl length $\lambda_P = \lambda_L^2/t$ (which is ≈ 800 nm in case of a 50 nm thick YBCO nanowire at $T = 4.2$ K)
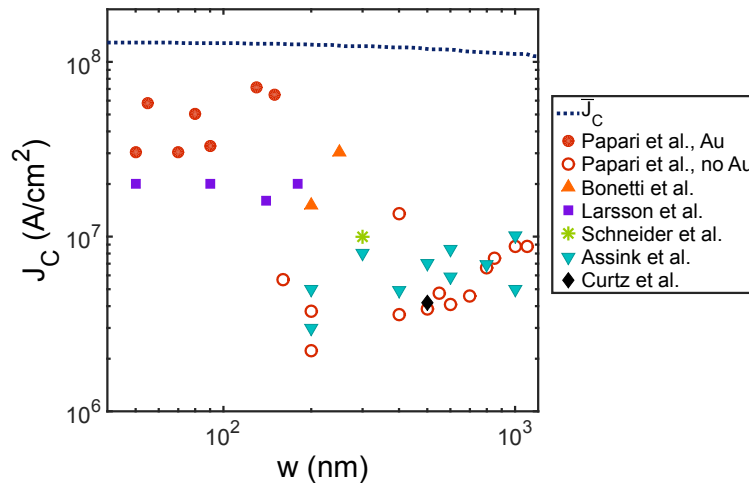
Figure 7. Critical current density J_C measured at 4.2 K as a function of the width w for different YBCO nanowires, available in literature [62, 63, 58, 22, 23, 49] (adapted from [62, 64]). The dotted line represents the numerically calculated critical current density $\bar{J}_C$ for an infinite long (type II) wire, with thickness $t < \lambda$, as a function of the width w. If $w < \lambda_P$, which is ≈ 800 nm for $t = 50$ nm, such a value saturates to the depairing limit.

and width much larger than ξ (as is the case for YBCO nanowires) is characterized by a uniform current distribution, with a J_C value only limited by the entry of Abrikosov vortices. When ramping up the bias current applied to a bridge, the critical supercurrent is reached once the local current density at the edges of the bridge equals a value close to the depairing current density [42]. At this point vortices can enter the bridge, causing a transition from the zero voltage state to the finite voltage state. Applying Eq.9 to the YBCO case at $T = 4.2$ K, one obtains a value of depairing current density $J_d \approx 1.3 \times 10^8$ A/cm^2 (with $\xi = 1.5$ nm and $\lambda_L = 230$ nm). The GL theory was developed for T close to T_C, however the results can be used also for lower T with a good approximation to experimental results.

A critical current density of the order of the above J_d value was never reported in literature previous to the development of the nanopatterning procedure described in section 3.1 and established in Ref.[29, 30]. In Fig.7 the main results from literature for J_C of nanowires as a function of width w are compared. Common features are a wide spread of the J_C values and a systematic decreasing of J_C when reducing the wire width. These features have been mainly attributed to damages occurring during the YBCO patterning.

In details, in Ref. [23] the authors find a steady reduction of the J_C from $w \approx 1~\mu$m till 200 nm with values never exceeding 10^7 A/cm^2 at 4.2 K. An almost constant J_C for nanowires in the range 50 nm $< w <$ 150 nm has been obtained in Ref. [58]. However in this case the maximum achieved J_C is of the order of 2×10^7 A/cm^2. Xu et al. [56], with their parallel arrays of hundreds of YBCO nanowires, have reached the ultimate lateral size, but at the expenses of the superconductivity. This is strongly affected by

the nanopatterning procedure, with average J_C for a single 15 nm wide wire as low as 10^5 A/cm^2 and a transition temperature below 20 K. In the attempt to improve the superconducting properties of YBCO nanowires, Papari et al. [62] made preliminary studies on the role of a protecting layer of Au. They obtained substantial improvement in the performances of the nanostructures and reported on nanowires ($w \approx 150$ nm wide) with J_C as high as 7×10^7 A/cm^2. However, for narrower wires they still observed a decreasing J_C, with values not exceeding 3×10^7 A/cm^2 for 50 nm wide wires. More importantly, in their work the narrower nanowires showed a transition temperature several degrees lower compared to the larger ones. This indicates significant damages of the smallest nanowires, possibly due to a too thin Au protecting layer of only 20 nm and to non-optimal Ar$^+$ ion milling parameters.

Recent advances in nano processing of YBCO films, described in section 3.1, made possible the realization of YBCO nanowires with cross sections as small as 50×50 nm^2 without degradation of the superconducting properties. Nawaz et al. [28] performed a systematic study of the critical current of YBCO nano bridges, patterned from 50 nm thick YBCO films, as a function of width ranging from 2 μm to 50 nm. All bridges could be characterized by a (local) critical current density approaching the Ginzburg Landau depairing critical current density, $J_d \simeq 1.3 \times 10^8$ A/cm^2, down to cross sections of 50×50 nm^2.

4. Nanowire-based nanoSQUIDs

Nanowire-based nanoSQUIDs are attractive due to their simpler fabrication process, compared to the grain boundaries based ones, and to the freedom to place them arbitrarily on a substrate. The performances, in terms of magnetic flux noise, have made these devices promising candidates to substitute state-of-the-art grain boundary junction based nanoSQUIDs [65, 66]. Hence, a lot of effort has been invested in the recent years to improve the noise level of nanowire-based nanoSQUIDs. In the following section, the nanoSQUID basic mechanisms are introduced and the performance of nanowire based devices are compared to the state-of-the-art technologies. Recent improvements in the nanoSQUID noise level, by e.g. removing the Au capping layer, are also discussed.

4.1. Critical Current Modulation of nanowire-based SQUIDs

The dc-SQUID consists of two weak links in a superconducting loop (see Fig. 8).

The total current through the SQUID is given by the sum of the currents flowing through each weak link

$$I_{\text{SQUID}} = I_1 f(\varphi_1) + I_2 f(\varphi_2) \, . \tag{19}$$

where $I_{1,2} f(\varphi_{1,2})$ are the 2π periodic current phase relations of the two weak links given by Eq.10 (see Fig.3). The two phase differences φ_1 and φ_2 are related to each other
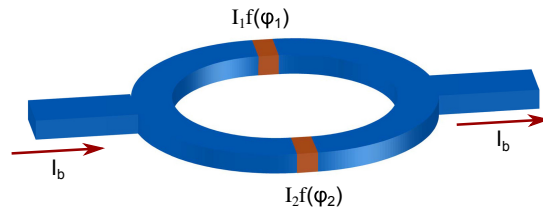
Figure 8. Sketch of a DC SQUID. The blue parts represent the superconducting electrodes. The short brown parts interrupting the SQUID loop are the weak links between the electrodes characterized by the current phase relations $I_{1,2}f(\varphi_{1,2})$, respectively.

through the fluxoid quantization [67]. Neglecting the contribution of the inductance of the SQUID arms one obtains

$$2\pi n = \varphi_1 - \varphi_2 + 2\pi \frac{\Phi}{\Phi_0} \; , \tag{20}$$

where Φ is the externally applied magnetic flux and n is an integer number. For a fixed Φ value, one can numerically calculate the maximum critical current flowing through the SQUID. This is done by maximizing Eq.19 with respect to e.g. φ_1 and considering the constraint given by Eq.20.

In Fig. 9 (a) the calculated critical current as a function of an externally applied magnetic flux is shown for various lengths of the weak link ranging from $l/\xi = 10$ to $l/\xi = 50$. Here we assumed that the vortex entry occurs at 0.6 I_d, where I_d is the depairing current of the individual weak links. The extracted relative modulation depth is shown in Fig. 9 (b). The critical current modulation pattern has strong similarities with a conventional SQUID, i.e. with weak links having a sinusoidal CPR, and having a screening parameter $\beta_\mathrm{L} = I_\mathrm{C}^{\max} L / \Phi_0$ larger than one [68]. Here I_c^{max} is the maximum critical current of the SQUID and L is the inductance of the SQUID loop. For nanowire-based nanoSQUIDs the value of SQUID inductance is generally dominated by the kinetic inductance of the weak links [69] and one can approximate the relative modulation depth $1/\beta_\mathrm{L}$ (solid line in Fig. 9 (b)) by replacing the expression of the loop inductance L with $2L_\mathrm{k}$, where L_k is the kinetic inductance of the individual nanowire weak link (see Eq.11)

$$\frac{\Delta I_\mathrm{C}}{I_\mathrm{C}^{\max}} \simeq \frac{1}{\beta_\mathrm{L}} = \frac{\Phi_0}{2L_\mathrm{k}I_\mathrm{C}^{\max}}. \tag{21}$$

This dependence is in agreement with calculations performed by Tesche and Clarke [68] for conventional SQUIDs (sinusoidal CPR weak links) with finite SQUID loop inductance.
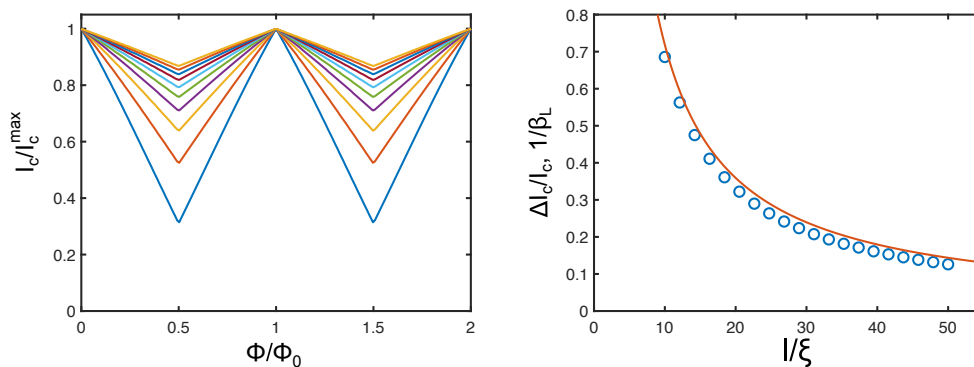
Figure 9. (a) Modulation of the critical current as a function of the applied magnetic flux of nanoSQUIDs for various lengths of the weak link ranging from $l/\xi = 10$ to 50 with equidistant steps (from bottom to top). (b) Relative modulation depth extracted from panel (a) as a function weak link length l/ξ (open symbols). The solid line represents the $1/\beta_{\mathrm{L}}$ calculated using Eq.21

## 4.2. Temperature dependence of critical current modulations

One of the main advantages of HTS based nanoSQUIDs is the extended temperature range of operation since, in most cases (as in the case of the device in Fig.10(a)), the devices show I_{C} modulations above $T = 77$ K. This opens the way to new experiments in a wide temperature and magnetic field range (the latter is due to high H_{C} in HTS). In the following we will discuss the temperature dependence of the critical current modulations as a function of an externally applied magnetic field.

In Figure 10(a) a SEM image of a YBCO nanowire based nanoSQUID is shown. The I_{C} modulations as a function of magnetic field, introduced in the previous section, have been measured on this device at various temperatures. As example, the I_{C} modulations measured at $T = 300$ mK are reported in Fig.10(b).

As discussed above, the critical current modulation depth strongly depends on the value of the wire inductances. When the nanowire lateral size is reduced down to the nanoscale, the kinetic inductance $L_{\mathrm{k}}(T)$ dominates the total inductance of the nanowires [69]. For example, as shown in Ref.[4], the value of kinetic inductance at 300 mK is already one order of magnitude higher than the geometric one at 4 K.

As shown in Eq.21, $\Delta I_{\mathrm{C}} \propto 1/L_{\mathrm{k}}$, hence, the experimentally measured ΔI_C is directly connected to the inductance of the nanoSQUID. The inductance of a nanoSQUID loop $L_{\mathrm{loop}}(T)$ (including the inductive contribution of the wires) can be numerically calculated by solving the Maxwell and London equations on the SQUID geometry [70]. Since L_{k} is strongly dependent on the London penetration depth λ_{L}, to obtain the temperature dependence of the SQUID inductance one can use the two-fluid model for $\lambda_{\mathrm{L}}(T)$ [67] and obtain

$$\lambda_{\mathrm{L}}(T) = \lambda_0 \frac{1}{\sqrt{1 - \left(\frac{T}{T_{\mathrm{C}}}\right)^2}} \; . \tag{22}$$
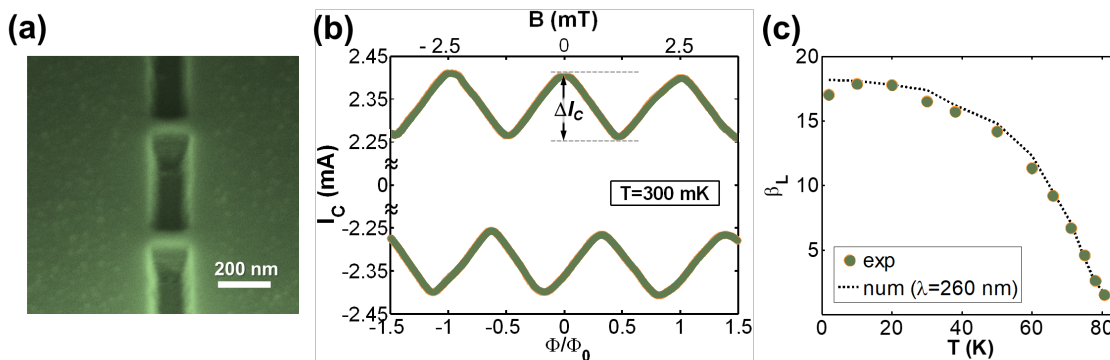
Figure 10. (a) Scanning electron microscope picture, in false colors, of a typical nanowire based nanoSQUID. (b) Critical current modulations at $T = 300$ mK for the nanoSQUID shown in panel (a) as a function of an externally applied magnetic flux. (c) Screening parameter β_{L} as a function of temperature. The experimental values of β_{L} (dots) have been determined using $\Delta I / I_{\mathrm{C}}^{\mathrm{max}}$ measured on the same device from panel (a) at various T. The experimental values of β_{L} can be fitted with a numerical calculated screening parameter according to Eq.23, shown as a dashed line.

The numerically calculated loop inductance $L_{\mathrm{loop}}^{\mathrm{num}}(T)$ allows to determine a numerical β_{L} through Eq.21, as

$$\beta_{\mathrm{L}}^{\mathrm{num}}(T) = \frac{I_{\mathrm{C}}^{\mathrm{max}}(T) L_{\mathrm{loop}}^{\mathrm{num}}(T)}{\Phi_0} \ . \tag{23}$$

In this expression, the values of $I_{\mathrm{C}}^{\mathrm{max}}(T)$ are extracted from the measurements. One can use the expression for $\beta_{\mathrm{L}}^{\mathrm{num}}(T)$ to fit the temperature dependence of the experimentally determined parameter, β_{L}^{exp} (see solid symbols in Fig.10(c)), defined through Eq.22 as

$$\beta_{\mathrm{L}}^{\mathrm{exp}}(T) = \frac{I_{\mathrm{C}}^{\mathrm{max}}(T)}{\Delta I_{\mathrm{C}}(T)} \ , \tag{24}$$

by using λ_0 as the only fitting parameter. This approach has been used to fit the data shown in Fig.10(c). Here $\beta_{\mathrm{L}}^{\mathrm{exp}}(T)$ has been determined from the critical current modulation as a function of an externally applied magnetic field for various temperatures. $\beta_{\mathrm{L}}^{\mathrm{num}}(T)$ has been numerically calculated and fitted to the experimental data. The best fit was obtained using $\lambda_0 = 260$ nm, which is a typical value for optimally doped YBCO thin films [62, 71].

4.3. Noise properties of nanowire-based SQUIDs

4.3.1. White magnetic flux noise As for any detector, the knowledge of the noise properties is fundamental to establish the possible applications of the SQUID. Since the SQUID is a magnetic flux detector, one is mainly interested in the modelling of the magnetic flux noise such that it would be possible to optimize the device performances.

The white flux noise limiting the performance of a DC-SQUID originates from thermal current noise (Johnson-Nyquist noise) of the weak link resistance R. For

optimized SQUID parameters $\beta_L \simeq 1$ and $\beta_C = 2\pi I_C R^2 C / \Phi_0 \lesssim 1$ (non-hysteretic current voltage characteristic), with C the capacitance of the weak links one obtains for the corresponding flux noise $S_\Phi^{1/2}$ of the SQUID [68]

$$S_\Phi^{1/2} = L\sqrt{\frac{16k_B T}{R}}, \tag{25}$$

where L is the inductance of the SQUID loop. One can clearly identify that the white flux noise will be limited by the loop inductance and the weak link resistance. This means that small loop inductances, i.e. small loop sizes, and high resistive weak links are preferably used to reach the lowest white flux noise in a SQUID.

4.3.2. $1/f$ *Magnetic flux noise* Noise power spectra proportional to $1/f$ at low frequencies are observed in many different physical systems and devices based on various materials, including semiconductors, normal metals and superconductors. Moreover, the $1/f$ noise intensity depends not only on the material but also on the technological methods used to realize the different devices.

As regards DC-SQUIDs, the origin of $1/f$ magnetic flux noise is not fully understood yet. The fact that the magnitude does not depend on the SQUID area, the superconducting thin film and the substrate used, strongly indicates that $1/f$ flux noise originates locally. A possible model has been proposed by Koch et al.[72], according to which, electrons can hop on and off from traps, mainly localized above and below the SQUID loop. Each trap locks the electron spin in a specific direction, which randomly varies from trap to trap. Uncorrelated changes of the spins directions result in a series of random telegraph noise (RTN), characterized by a Lorentzian power spectrum, which sum to a total $1/f$ power spectrum. Other models have been proposed, such as: electron spin diffusion [73], magnetic moments locally originated in metal induced gap states [74] and paramagnetic moments from localized electrons resulting in a $\propto 1/T$ temperature dependence of the power spectrum intensity [75]. The latter dependence has been recently observed over a range of frequency around 1 GHz, from the measurement of a tunable gap flux qubit [76]. In the case of HTS SQUIDs, operated at $T = 77$ K, $1/f$ magnetic flux noise has been also associated to thermal activation of vortex motion between different pinning sites. By reducing the device lateral dimensions below $\sqrt{\Phi_0/B}$, where B is the field in which the SQUID is cooled down, this noise source can be eliminated. However, the fact that such $1/f$ behavior is also observed at lower temperatures suggests that a different mechanism is responsible for it.

4.3.3. Critical current noise Critical current fluctuations in Josephson junctions are commonly attributed to charge trapping at defect sites in the junction barrier [77]. Since charge traps are commonly assumed to be local and non interacting, their distribution produces a sum of Lorentzian features, resulting in $1/f$ noise power spectrum [78]. Critical current noise with characteristic $1/f$ spectrum has also been observed in YBCO nanowire based nanoSQUIDs [4, 32]. However, for nanowires the microscopic origin of

this noise is still unknown. Here, critical current noise could possibly be caused by fluctuations of the electronic nematic order [79, 80] or by changes in the oxygen order and concentration in the CuO chains [81], resulting in a variation of the energy barrier for the vortex entry dynamics in the nanowires [43]. Systematic studies (including geometry and temperature dependencies) are still needed for a full understanding of the physical mechanisms responsible for such behavior. The effect of the critical current fluctuations on the total voltage noise in SQUID applications can be minimized by the use of a bias reversal scheme for the SQUID readout [82]. With bias reversal, the working point is periodically varied in a closed loop, including four different combinations of current and flux bias.

4.3.4. Au capped YBCO nanoSQUIDs A thin layer of Au, introduced as a capping layer to preserve the YBCO films, leads to a significant improvement of nanowire properties [28, 29, 30] and enables the fabrication of nanowire based nanoSQUIDs with ultra-low magnetic flux noise[4].
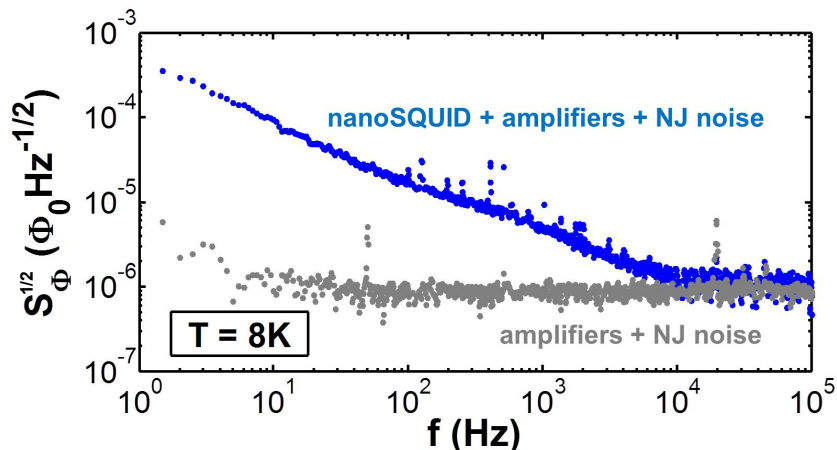
Figure 11. Flux noise spectral density vs. frequency measured at $T = 8$ K on a nanoSQUID on a (110) MgO substrate and with a geometrical loop area $A_g = 0.1~\mu m^2$.

The lowest reported white magnetic flux noise for Au capped YBCO nanowire based nanoSQUIDs is $S_\Phi^{1/2} \simeq 1~\mu\Phi_0/\sqrt{Hz}$ [4] (see Fig. 11). This is among the lowest reported values for YBCO nanoSQUIDs and opens the possibility for the study of magnetic nanoparticles in a wide temperature and magnetic field range. The magnetic flux noise can be used to calculate the spin sensitivity of the nanoSQUID as $S\mu^{1/2} = S_\Phi^{1/2}/\phi_\mu$, where ϕ_μ is a coupling factor obtained from simulations [83]. For the nanoSQUID presented in Ref. [30], the spin sensitivity has been reported to be $S\mu^{1/2} = 50~\mu_B/\sqrt{Hz}$, where μ_B is the Bohr magneton. The lowest spin sensitivity reported for YBCO nanoSQUIDs is $S\mu^{1/2} = 3.7~\mu_B/\sqrt{Hz}$, obtained with grain boundary junctions [65].

Although nanoSQUIDs have reached very low levels of magnetic flux noise, their sensitivity is still far from making possible the detection of a single spin. To reach the ultimate quantum limit of nanoSQUID sensitivity, their performances need to be further

improved. It has been reported that in most nanowire-based nanoSQUIDs measurements [4, 15, 32], the white noise level is limited by the read out electronics input voltage noise $S_V^{1/2}$. The corresponding flux noise is given by $S_\Phi^{1/2} = S_V^{1/2}/V_\Phi$, where the transfer function V_Φ is the maximum derivative of the SQUID output voltage modulations as a function of magnetic flux.

Therefore, in order to mitigate the noise contribution from the electronics one needs to increase the value of transfer function V_Φ. Since the latter is defined as $V_\Phi = max(\frac{\delta V}{\delta \Phi})$, and assuming a sinusoidal behavior of $V(\Phi)$, the transfer function can be approximated as $V_\Phi \approx \pi \Delta V$. Here, ΔV is the maximum voltage modulation depth and can, in turn, be approximated to $\Delta V \approx \delta R \Delta I$. Here ΔI is the critical current modulation depth and δR is the differential resistance of the weak link at the operating current biasing point (typically slightly above the critical current). From this relation, we can see that in order to increase the voltage modulation depth, one must increase the critical current modulation depth and/or the differential resistance. The former has been discussed in section 4.1, we will now focus on the improvement of ΔV via the increase of δR.

A first solution is to remove the Au capping from the nanowire. While the Au protects the YBCO nanowires during fabrication, it also acts as a low resistive shunt of the weak links, strongly reducing δR. The effect of the gold layer has been analyzed in Ref.[30]. The fabrication presented in section 3.1 has been improved by removing the Au capping. The reported results have shown that uncapped nanowires retain pristine quality [31, 32] with critical current density slightly lower than nanowires with gold capping. Moreover, nanoSQUIDs fabricated without Au have been compared to Au-capped nanoSQUIDs and demonstrated a two fold increase of the transfer function due to an increased δR [32]. Another significant improvement to the differential resistance can be achieved by reducing the thickness of the YBCO nanowire, which will be discussed in more detail in the next section.

4.3.5. Ultra-thin YBCO nanoSQUIDs The lowest magnetic flux noise measured on nanoSQUIDs based on YBCO nanowires has been achieved by implementing ultra-thin Dayem bridges. It has been shown that by reducing the thickness of the nanowires, t, it is possible to reach white magnetic flux noise as low as $S_\Phi^{1/2} = 450 \, n\Phi_0/\sqrt{Hz}$ at $T = 18$ K [32]. This is more than a two fold improvement compared to the nanoSQUIDs reported in the previous section. A summary of device parameters and performances for YBCO nanoSQUIDs of various thickness are shown in Table 1. The improvement of nanoSQUID performances when reducing t is due to increase of the differential resistance. This is most prominent for $t < 15$ nm, where the structure can be considered almost 2D [84]. In this limit, it has been shown that the normal state sheet resistance $R_\square$ of YBCO does not scale as $1/t$ (as expected for the 3D case), but instead increases faster than $1/t$ for decreasing thickness [85, 86, 87]. $R_\square$ is related directly to δR and, as can be seen from table 1, both increase significantly for thinner nanowires.

Removing the protective Au capping demonstrates that high quality nanowires can be obtained and used for nanoSQUIDs with I_C modulation in the entire temperature

range, up to $T_C \simeq 83$ K [32]. The resulting δR of ultra-thin nanowires without gold is almost 10 times higher compared to capped nanowires with comparable thickness.

Device	Au	t (nm)	w (nm)	l (nm)	I_C (μA)	J_C (A/cm²)	β_L	δR (Ω)	$R_\square$ (Ω)	ΔV_{max} (mV)	V_Φ (mV/Φ_0)	$S_{\Phi,w}^{1/2}$ ($\mu\Phi_0/\sqrt{Hz}$)
NSQ10	No	10	75	100	130	$1.0 \cdot 10^7$	23	110	130	0.65	3.6	<0.45
NSQ20	No	20	65	100	580	$2.2 \cdot 10^7$	24	19	33	0.45	2.7	-
NSQ50	No	50	65	100	1000	$1.5 \cdot 10^7$	20	13	12	0.42	2.2	<0.6
NSQR	Yes	50	65	100	2220	$3.4 \cdot 10^7$	18	1.5	4	0.2	1.5	<1

Table 1. (Adapted from [32])Parameters of some investigated Dayem bridge nanoSQUIDs for various thicknesses t. The wire lengths l and widths w are obtained from SEM imaging. All SQUIDs are without any Au capping except device NSQR, which is reported here for comparison. I_C, J_C, β_L and $\delta R = \partial V/\partial I$ are, respectively, the critical current of the device, the critical current density of the wires, the screening parameter, and the differential resistance, extracted from the IV characteristics at 4.2 K, with a voltage criterion of V=2 μV. $R_\square$ is the sheet resistance of the devices, measured at $T = 100$ K. ΔV_{max} is the maximum amplitude of the voltage modulations as a function of the externally applied magnetic field, at a given bias current. V_Φ is the value of the transfer function at the working point used for the noise measurement. $S_{\Phi,w}$ is the white magnetic flux noise upper limit of the device, as set by the electronics background noise. ΔV_{max}, V_Φ and $S_{\Phi,w}$ are measured at 4.2 K for devices NSQ20, NSQ50 and NSQR, while they are measured at 18 K for NSQ10.

5. Nanowire-based magnetometers

So far, we have discussed nanoSQUID properties with focus on the magnetic flux sensitivity of the devices. Since the flux noise depends on the total inductance of the device, a nanometer sized loop is preferable for applications such as magnetization measurements and magnetic nanoparticle studies [8, 6]. On the other hand, the use of SQUID as magnetometers requires an improved magnetic field sensitivity. SQUID based magnetometers are extensively used in magneto-encephalography [88, 16], low field magnetic resonance imaging[89] and geophysical surveys [90]. For these applications, devices with low magnetic field noise are required: $S_B^{1/2} = S_\Phi^{1/2}/A_{eff}$, where A_{eff} is the effective area of the device. Generally, nanoSQUIDs have a poor magnetic field sensitivity because of their intrinsically small size, i.e. small A_{eff}. In order to take advantage of the low flux noise (small loop area), one can directly couple the nanoSQUID to a much larger pickup loop: this significantly increases A_{eff} while maintaining low $S_\Phi^{1/2}$, hence improving the magnetic field sensitivity. The pickup loop approach is preferable over a SQUID washer design [91], since the implementation of a large washer to enhance A_{eff} will, at the same time, also increase the SQUID inductance. Moreover, fabrication of a pickup loop generally involves only a single layer patterning, making it simpler than, e.g., an inductively coupled multiturn flux transformer. NanoSQUIDs based on YBCO nanowires directly coupled to a pickup loop have been realized with promising results [15, 16]. In the following, the effect of the pickup loop on the effective area will

be analyzed and the magnetic field noise performances of nanowire based nanoSQUIDs compared to other magnetometers.

5.1. Effective area of YBCO nanoSQUIDs coupled to a pickup loop

The effective area, A_{eff}, is a key parameter to determine the performances of a SQUID magnetometer. A_{eff} represents the portion of the device that contributes to magnetic flux when an external magnetic field B_{a} is applied. Compared to grain boundaries devices, for nanowire based SQUIDs the kinetic inductance has a strong influence on the final value of effective area, as will be discussed later. Even in the absence of a pickup loop, the effective area of a nanoSQUID is larger than the geometrical one A_{geo}. This is due to the extra phase gradient in the two electrodes, generated by the screening current I_{s} induced by the externally applied magnetic field. In the limit $t \leq \lambda_{\text{L}}$, it can be shown numerically that [4]

$$A_{\text{eff}} \simeq d_{\text{w}} \times w_{\text{e}}, \tag{26}$$

where d_{w} is the separation distance between the two nanowires and w_{e} the electrode width. A similar relation was found analytically in Ref.[9].

As mentioned above, a large effective area is desirable for a nanoSQUID since it results in lower field noise, provided that the value of the magnetic flux noise, $S_{\Phi}^{1/2}$, is independent of A_{eff}. As it can be seen from equation 26, in order to get a larger A_{eff}, one should implement wider electrodes and/or increase the nanowires distance d_{w}. However, this would result in significant increase of $S_{\Phi}^{1/2}$, since a nanosized SQUID loop is one of the main responsible for low flux noise. So, in order to increase the field sensitivity, one must increase A_{eff} without at the same affecting negatively $S_{\Phi}^{1/2}$. A solution is to employ a large pickup loop inductively coupled to the small SQUID loop [15, 16].

This kind of device can be represented with an equivalent circuit where the nanowires and the pickup loop act as inductors, as shown in Fig. 12(a). In this representation, the effect of the pickup loop on A_{eff} can be determined using an interacting loop-current model for superconducting networks in the presence of an externally applied magnetic field and satisfying the fluxoid quantization condition[92]. As described in Ref. [15], one obtains the following expression for the effective area of the device

$$A_{\text{eff}} = A_{\text{eff}}^{\text{nS}} + A_{\text{eff}}^{\text{pl}} \frac{L_{\text{c}}}{L_{\text{pl}}}, \tag{27}$$

where $A_{\text{eff}}^{\text{nS}}$ and $A_{\text{eff}}^{\text{pl}}$ are the effective areas of the nanoSQUID loop and of the pickup loop respectively, L_{c} and $L_{\text{pl}} = L_{\text{loop}}^{1} + L_{\text{loop}}^{2} + L_{\text{c}}$ are the coupling and the total pickup loop inductance, respectively. As it infers from Eq.27, the coupling inductance L_{c} plays the major role in the final value of the effective area.

An example of a nanoSQUID with integrated pickup loop is shown in Fig.12(b), adapted from Ref.[15]. To further increase the coupling inductance L_{c}, the SQUID loop
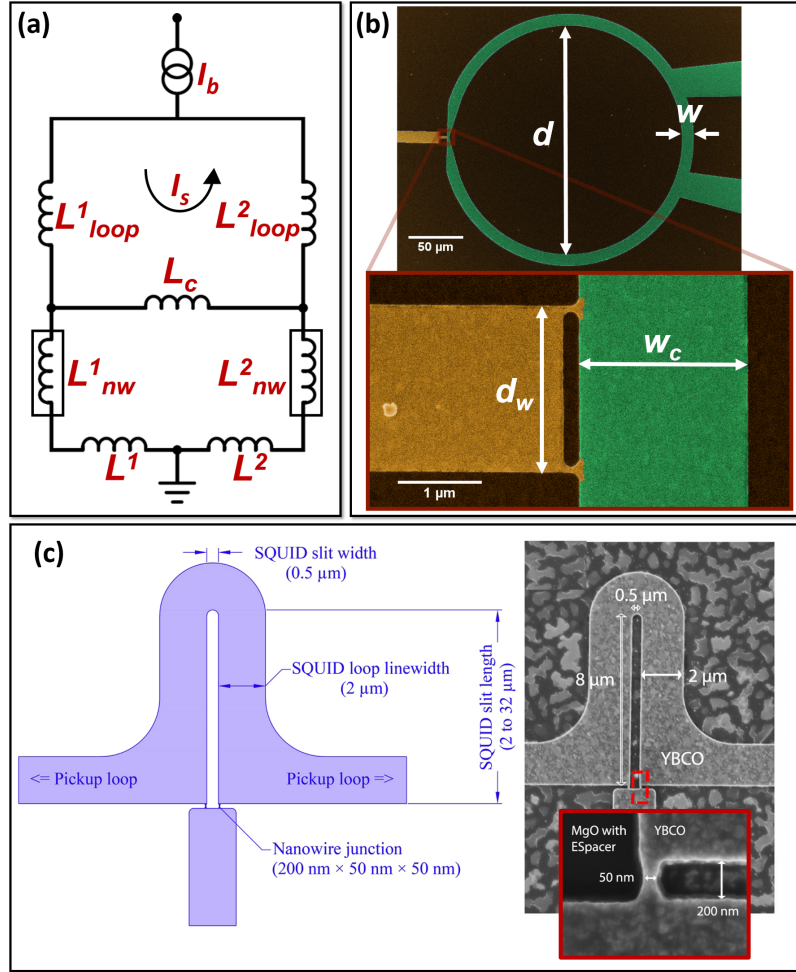
Figure 12. (a) Circuit network schematic of a nanowire based nanoSQUID galvanically coupled to a pickup loop. L_c is the coupling inductance. The nanowires are represented by the inductances L_{nw}^1 and L_{nw}^2. The pickup loop inductance is given by the sum $L_{pl} = L_c + L_{loop}^1 + L_{loop}^2$ and the nanoSQUID loop inductance by the sum $L_{nw}^1 + L_{nw}^2 + L_c + L^1 + L^2$. I_b and I_s are respectively the bias and the screening current. (b) (adatpted from [15]) SEM image in false colors of a YBCO nanowire based magnetometer implementing a pickup loop. The inset shows the nanoSQUID (c) (adapted from [16]) Schematic and SEM image of nanoSQUID magnetometers with hairpin SQUID loop design to increase the coupling inductance L_c.

can be modified, as shown in Fig.12(c). Here the elongated SQUID loop significantly increases the coupling to the pickup loop, enhancing A_{eff} [16].

An analytical expression for the effective area can be obtained from Eq.27 using the following expressions for the SQUID inductance. Here we include both the geometric (L_{ex}) and the kinetic (L_{kin}) contributions to the pickup loop L_{loop} and the coupling L_c inductance[93]

$$L'_{\text{loop}} = \frac{\mu_0 \lambda_{\text{L}}}{w} \coth\left(\frac{t}{\lambda_{\text{L}}}\right) + \frac{\mu_0}{2\pi}\left[\ln\left(\frac{16r}{w}\right) - 2\right] \tag{28}$$
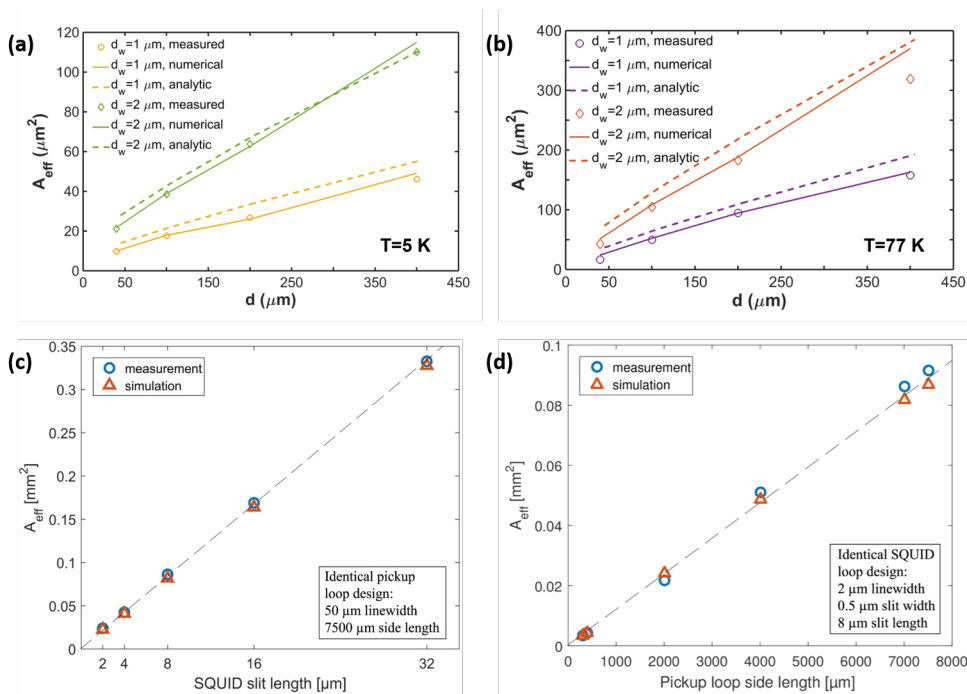
Figure 13. Experimental effective area (open light blue circles) as function of the pickup loop diameter d(see Fig.12(b)), at $T = 5$ K (a) and $T = 77$ K (b) for two SQUIDs having different distances d_w between the nanowires (adapted from [15]). (c) A_{eff} as a function of SQUID slit length (see Fig. 12(c)). (d) A_{eff} as a function of pickup loop lateral dimension for SQUID magnetometers with SQUID slit length of 8 μm (see Fig.12(c)). ((c) and (d) are adapted from [16]).

$$L'_{\mathrm{c}} = \frac{\mu_0 \lambda_{\mathrm{L}}}{w_{\mathrm{c}}} \coth\left(\frac{t}{\lambda_{\mathrm{L}}}\right) + k/2. \tag{29}$$

where w and r are the line width and average radius of the pickup loop respectively, and w_{c} is the width of the YBCO strip where the two loops meet (see Fig.12(b)). $k \simeq 0.3$ pH/μm is an empirical expression for a slit inductance per unit length, obtained from measurements and simulations[94]. The geometric term of L'_{c} is then approximated as half slit inductance. The prime sign indicates that equations 28 and 29 are per unit length.

Figures 13(a) and (b) show the measured effective areas of nanoSQUID-based magnetometers depicted in Fig.12 [15]. Here, the experimentally determined effective area $A_{\mathrm{eff}}^{\mathrm{exp}}$ is shown versus the pickup loop diameter d, for nanoSQUIDs with nanowire separation $d_w = 1$ μm (open circles) and $d_w = 2$ μm (diamonds), both at $T = 5$ K and at $T = 77$ K. The solid and the dashed lines represent the numerically ($A_{\mathrm{eff}}^{\mathrm{num}}$) and the analytically calculated ($A_{\mathrm{eff}}^{\mathrm{an}}$) effective areas respectively.

Here the numerical calculations were performed by solving the Maxwell London equations on the specific SQUID geometries [15]. The best fitting of $A_{\mathrm{eff}}^{\mathrm{exp}}$ has been obtained for $\lambda_0 = 150$ nm at $T = 5$ K, and $\lambda_L(T = 77$ K$) \approx 400$ nm, and using Eq.22 with $T_c = 83$ K and $n = 2$. The approximately fourfold increase of effective area

when increasing the temperature from 5 K to 77 K can be attributed to the increase of coupling inductance, which is dominated by the kinetic term. In fact, the kinetic inductance diverges when approaching T_C.

In Fig.13 (c) and (d) the experimental and simulated values of effective area of YBCO nanoSQUID-based magnetometers are shown [16]: the values of the coupling inductance are higher than those reported by Arzeo et. al [15], and the pickup loop is bigger (see Fig.13 (a) and (b)). Both the increment of the SQUID hairpin slit length to 32 μm (see Fig. 12) and the size of the pickup loop (square pickup loop with lateral dimension of 7.5×7.5 mm^2) result in effective areas up to 0.34 mm^2.

In the work of Xie et al. [16], the inductance of the nanowires contribute considerably to the total SQUID loop inductance. In fact, for slit lengths above 8 μm a suppression of ΔV due to the increased SQUID inductance has been reported. This sets a limit to the maximum coupling achievable, above which the voltage modulations of the SQUID are strongly suppressed by the SQUID loop inductance. This a common problem for SQUID magnetometers galvanically coupled to a pick up loop: the need for a larger A_{eff} usually requires a large coupling inductance (see Eq.27). However, the increase of the SQUID inductance results in smaller voltage modulation depths, hence in a higher flux noise.

5.2. Noise properties of nanowire-based magnetometers

The noise data reported by Arzeo et. al [15] indicate that the white magnetic flux noise of nanowire based YBCO nanoSQUIDs is not affected by the presence of a pickup loop. Therefore, the use of a larger pickup loop would in principal allow to improve the magnetic field sensitivity indefinitely. This technology has shown the potential to reach white magnetic noise levels below $S_{\text{B}}^{1/2} \approx 100$ fT/$\sqrt{\text{Hz}}$ [16], which represent a milestone for SQUID applications [88, 16, 89, 95].

We can compare the results reported on the magnetic field noise of nanowire-based SQUID magnetometer with the state-of-the-art HTS-based technology. As of today, the lowest reported magnetic field noise at $T = 77$ K for nanowire-based YBCO nanoSQUIDs is $S_{\text{B}}^{1/2} = 1.2$ pT/$\sqrt{\text{Hz}}$ (for a single layer device) and $S_{\text{B}}^{1/2} = 240$ fT/$\sqrt{\text{Hz}}$ (for flip-chip device coupled to a flux-transformer) [16]. At lower temperature, $T = 5$ K, a magnetic field noise as low as $S_{\text{B}}^{1/2} = 66$ pT/$\sqrt{\text{Hz}}$ was achieved [15]. This last result was obtained with a smaller A_{eff} compared to the SQUID magnetometers presented in [16], while the reported flux noise was lower than $S_{\Phi}^{1/2} = 1$ $\mu\Phi_0/\sqrt{\text{Hz}}$.

These results are not yet competitive with the state-of-the-art SQUID magnetometers. The lowest magnetic field noise has been reported for step-edge junction based SQUID magnetometers, having $S_{\text{B}}^{1/2} = 2$ fT/$\sqrt{\text{Hz}}$ at $T = 77$ K [96]. Here, a different and more advanced coupling scheme, i.e. a ferromagnetic flux antenna in combination with a flux transformer, was used. This resulted in a considerable increase of the effective area A_{eff} of the SQUID. Considering single layer SQUIDs, the lowest magnetic noise level has been reported for bicrystal grain boundary junction based

SQUIDs [97, 98]. These devices reached $S_{\mathrm{B}}^{1/2} = 30 - 40$ fT/$\sqrt{\mathrm{Hz}}$ with a pickup loop of 8×8 mm^2 galvanically coupled to the SQUID.

6. Conclusions and Outlook

The scope of this review is to give the reader an overview on YBCO nanowires and on their implementaion in HTS nanoSQUIDs.

In the first part, we have presented the theory developed to describe the physics of the nanowires, which is dominated by Abrikosov vortices, in order to better understand the differences between YBCO nanowires and other kind of weak links and junctions, which are commonly used in nanoSQUIDs.

In the second part, we have described the nanofabrication procedure which, up to now, has given the best results in terms of nanowire properties and performances: indeed, the properties of the bulk HTS material are preserved during the nanoprocessing, when YBCO is shrunk down to the nanoscale.

Finally, the pristine nanowires have been used in nanoSQUIDs. These devices work in the full temperature range up to T_{C}, exhibiting critical current modulations as a function of the external magnetic field, which have never been seen before for similar HTS devices. Moreover, they show record values for the white flux noise, making them very attractive for fundamental studies, ranging from nanomagnetism to spintronics, and applications such as spin-based quantum information processing and medical diagnostics.

At present, a grand effort is invested to improve the performance of YBCO nanoSQUIDs. One possible approach is to realize devices, where the feature (SQUID loop and weak links) size is minimized. Indeed a reduction of device dimensions would allow to further reduce the SQUID inductance, with a consequent improvement of flux noise. However, as shown in section 3.1, the fabrication of high quality HTS nanostructures is challenging, and with the current technology a further reduction in dimensions, while keeping unaltered the bulk properties, is not possible.

A different approach is to replace Dayem bridges with Variable Thickness Bridges (VTB) or ion irradiated bridges. This would result in an enhancement of the differential resistance δR of the weak links, which is a crucial parameter, as described in section 4.3.4. A δR increase would allow to improve the voltage modulation depth, therefore reducing significantly the flux noise of the SQUID.

During the early 1990's, a lot of attention was given to VTBs and ion damaged nanowires [99]. While VTB technology has been succesfully exploited for LTS, no results have been reported, in recent years, for HTS based VTBs. Several studies have been reported on YBCO JJs and SQUIDs using Focused Ion Beam milling (FIB). These results have shown the viability of FIB for fabricating high quality JJs [51] and nanoSQUIDs [2, 50]. In fact a reproducible fabrication process for variable thickness bridges would present a solution, which encompasses the flexible and scalable fabrication of nanowires, together with the superior performances, which are typical of Josephson

Junction based nanoSQUIDs.

Acknowledgements

Bibliography

[1] Hao L, Macfarlane J, Gallop J, Cox D, Beyer J, Drung D and Schurig T 2008 *Applied Physics Letters* **92** 192507

[2] Wu C H, Chou Y T, Kuo W C, Chen J H, Wang L M, Chen J C, Chen K L, Sou U C, Yang H C and Jeng J T 2008 *Nanotechnology* **19** 315304

[3] Vijay R, Levenson-Falk E, Slichter D and Siddiqi I 2010 *Applied Physics Letters* **96** 223112

[4] Arpaia R, Arzeo M, Nawaz S, Charpentier S, Lombardi F and Bauch T 2014 *Applied Physics Letters* **104** 072603

[5] Charpentier S, Arpaia R, Gaudet J, Matte D, Baghdadi R, Löfwander T, Golubev D, Fournier P, Bauch T and Lombardi F 2016 *Physical Review B* **94** 060503

[6] Wernsdorfer W 2001 *Advances in Chemical Physics* **118** 99–190

[7] Lam S and Tilbrook D 2003 *Applied physics letters* **82** 1078–1080

[8] Gallop J 2003 *Superconductor Science and Technology* **16** 1575

[9] Hopkins D S, Pekker D, Goldbart P M and Bezryadin A 2005 *Science* **308** 1762–1765

[10] Foley C and Hilgenkamp H 2009 *Superconductor science and technology* **22** 064001

[11] Bouchiat V 2009 *Superconductor Science and Technology* **22** 064002

[12] Granata C and Vettoliere A 2016 *Physics Reports* **614** 1–69

[13] Granata C, Esposito E, Vettoliere A, Petti L and Russo M 2008 *Nanotechnology* **19** 275501

[14] Troeman A G, Derking H, Borger B, Pleikies J, Veldhuis D and Hilgenkamp H 2007 *Nano Letters* **7** 2152–2156

[15] Arzeo M, Arpaia R, Baghdadi R, Lombardi F and Bauch T 2016 *Journal of Applied Physics* **119** 174501

[16] Xie M, Chukharkin M, Ruffieux S, Schneiderman J, Kalabukhov A, Arzeo M, Bauch T, Lombardi F and Winkler D 2017 *Superconductor Science and Technology* **30** 115014

[17] Braginski A 1993 Thin film structures *The New Superconducting Electronics* (Springer) pp 89–122

[18] Tafuri F and Kirtley J R 2005 *Reports on Progress in Physics* **68** 2573 URL http://stacks.iop.org/0034-4885/68/i=11/a=R03

[19] Koelle D, Kleiner R, Ludwig F, Dantsker E and Clarke J 1999 *Reviews of Modern Physics* **71** 631

[20] Martínez-Pérez M J and Koelle D 2016 *Physical Sciences Reviews* **2**

[21] Voss R F, Laibowitz R B and Broers A N 1980 *Applied Physics Letters* **37** 656–658

[22] Schneider J, Kohlstedt H and Wördenweber R 1993 *Applied physics letters* **63** 2426–2428

[23] Assink H, Harg A, Schep C, Chen N, Marel D, Hadley P, Drift E and Mooij J 1993 *IEEE transactions on applied superconductivity* **3** 2983–2985

[24] Barth R, Spangenberg B, Jaekel C, Roskos H G, Kurz H and Holzapfel B 1993 *Applied physics letters* **63** 1149–1151

[25] van der Harg A, van der Drift E and Hadley P 1995 *IEEE Transactions on Applied Superconductivity* **5** 1448–1451

[26] Schneider J, Mück M and Wördenweber R 1994 *Applied physics letters* **65** 2475–2477

[27] Pedyash M, Blank D H and Rogalla H 1996 *Applied physics letters* **68** 1156–1158

[28] Nawaz S, Arpaia R, Lombardi F and Bauch T 2013 *Physical review letters* **110** 167004

[29] Nawaz S, Arpaia R, Bauch T and Lombardi F 2013 *Physica C: Superconductivity* **495** 33–38

[30] Arpaia R, Nawaz S, Lombardi F and Bauch T 2013 *IEEE Trans. Appl. Supercond* **23** 1101505–1101505

[31] Trabaldo E, Arzeo M, Arpaia R, Baghdadi R, Andersson E, Lombardi F and Bauch T 2017 *IEEE Transactions on Applied Superconductivity* **27** 1–4

[32] Arpaia R, Arzeo M, Baghdadi R, Trabaldo E, Lombardi F and Bauch T 2016 *Superconductor Science and Technology* **30** 014008

[33] Clem J R and Kogan V 2012 *Phys. Rev. B* **86** 174521

[34] London F and London H 1935 *Proc. R. Soc. Lond. A* **149** 71–88

[35] Stewart W 1968 *Applied Physics Letters* **12** 277–280

[36] Aslamazov L and Lemnitskii S 1983 *Sov. Phys.-JETP (Engl. Transl.);(United States)* **57**

[37] Aslamazov L and Larkin A 1969 *ZhETF Pisma Redaktsiiu* **9** 150

[38] Likharev K and Iakobson L 1976 *Soviet Physics Technical Physics* **20** 1503–1509

[39] Langer J S and Ambegaokar V 1967 *Physical Review* **164** 498

[40] Likharev K 1979 *Reviews of Modern Physics* **51** 101

[41] Likharev K and Yakobson L 1976 *Sov. Phys.-JETP* **41** 570

[42] Vodolazov D Y, Maksimov I and Brandt E 1999 *Europhys. Lett.* **48** 313

[43] Bulaevskii L, Graf M, Batista C and Kogan V 2011 *Physical Review B* **83** 144526

[44] Kupriyanov M Y, Likharev K and Maslova L 1975 The jsub (s)(psi) relationship, abrikosov vortices and josephson vortices in variable thickness bridges *Low temperature physics*

[45] Bean C and Livingston J 1964 *Physical Review Letters* **12** 14

[46] Arpaia R, Golubev D, Baghdadi R, Arzeo M, Kunakova G, Charpentier S, Nawaz S, Lombardi F and Bauch T 2014 *Physica C* **506** 165–168

[47] Baghdadi R, Arpaia R, Bauch T and Lombardi F 2015 *IEEE Trans. Appl. Supercond* **25**

[48] Baghdadi R, Arpaia R, Charpentier S, Golubev D, Bauch T and Lombardi F 2015 *Physical Review Applied* **4** 014022

[49] Curtz N, Koller E, Zbinden H, Decroux M, Antognazza L, Fischer Ø and Gisin N 2010 *Superconductor Science and Technology* **23** 045015

[50] Wu C H, Jhan F J, Chen J H, Jeng J T, Chen K L and Yang H C 2011 *IEEE Transactions on Applied Superconductivity* **21** 375–378

[51] Cybart S A, Cho E, Wong T, Wehlin B H, Ma M K, Huynh C and Dynes R 2015 *Nature nanotechnology* **10** 598

[52] Cho E Y, Zhou Y W, Cho J Y and Cybart S A 2018 *Applied Physics Letters* **113** 022604

[53] Zhang G, Lu X, Zhang T, Qu J, Wang W, Li X and Yu S 2006 *Nanotechnology* **17** 4252

[54] Morales P, DiCiano M and Wei J 2005 *Applied Physics Letters* **86** 192509

[55] Mansour A, Chow K and Jung J 2011 *Journal of Applied Physics* **110** 063909

[56] Xu K and Heath J R 2008 *Nano letters* **8** 3845–3849

[57] Elkaseh A, Perold W and Srinivasu V 2010 *Journal of Applied Physics* **108** 053914

[58] Larsson P, Nilsson B and Ivanov Z 2000 *Journal of Vacuum Science & Technology B: Microelectronics and Nanometer Structures Processing, Measurement, and Phenomena* **18** 25–31

[59] Gustafsson D, Lombardi F and Bauch T 2011 *Physical Review B* **84** 184526

[60] Stornaiuolo D, Rotoli G, Cedergren K, Born D, Bauch T, Lombardi F and Tafuri F 2010 *Journal of Applied Physics* **107** 113901

[61] Tahara S, Anlage S M, Halbritter J, Eom C B, Fork D, Geballe T and Beasley M 1990 *Physical Review B* **41** 11203

[62] Papari G, Carillo F, Stornaiuolo D, Longobardi L, Beltram F and Tafuri F 2012 *Superconductor Science and Technology* **25** 035011

[63] Bonetti J, Van Harlingen D and Weissman M 2003 *Physica C: Superconductivity* **388** 343–344

[64] Arpaia R 2016 $YBa_2Cu_3O_{7-\delta}$ *Nanowires to Study Nanoscale Ordering in High-T_C Superconductors* (PhD thesis, Department of Microtechnology and Nanoscience, Chalmers University of

Technology)

[65] Schwarz T, Wölbing R, Reiche C F, Müller B, Martínez-Pérez M J, Mühl T, Büchner B, Kleiner R and Koelle D 2015 *Physical Review Applied* **3** 044011

[66] Schwarz T, Nagel J, Wolbing R, Kemmler M, Kleiner R and Koelle D 2012 *ACS nano* **7** 844–850

[67] Tinkham M 2004 *Introduction to Superconductivity* (Dover Publications) ISBN 9780486435039 URL http://books.google.it/books?id=k6AO9nRYbioC

[68] Tesche C D and Clarke J 1977 *Journal of Low Temperature Physics* **29** 301–331

[69] Hasselbach K, Mailly D and Kirtley J 2002 *Journal of applied physics* **91** 4432–4437

[70] Khapaev Jr M 1997 *Superconductor Science and Technology* **10** 389

[71] Arpaia R, Andersson E, Trabaldo E, Bauch T and Lombardi F 2018 *Physical Review Materials* **2** 024804

[72] Koch R H, DiVincenzo D P and Clarke J 2007 *Physical review letters* **98** 267003

[73] Faoro L and Ioffe L B 2008 *Physical review letters* **100** 227005

[74] Choi S, Lee D H, Louie S G and Clarke J 2009 *Physical review letters* **103** 197001

[75] Sendelbach S, Hover D, Mück M and McDermott R 2009 *Physical review letters* **103** 117001

[76] Quintana C, Chen Y, Sank D, Petukhov A, White T, Kafri D, Chiaro B, Megrant A, Barends R, Campbell B *et al.* 2017 *Physical review letters* **118** 057702

[77] Van Harlingen D, Robertson T, Plourde B, Reichardt P, Crane T and Clarke J 2004 *Physical Review B* **70** 064517

[78] Rogers C and Buhrman R 1984 *Physical review letters* **53** 1272

[79] Loh Y, Carlson E and Dahmen K 2010 *Physical Review B* **81** 224207

[80] Carlson E and Dahmen K 2011 *Nature communications* **2** 379

[81] Scouten S, Xu Y, Moeckly B and Buhrman R 1994 *Physical Review B* **50** 16121

[82] Drung D 2003 *Superconductor Science and Technology* **16** 1320

[83] Nagel J, Konovalenko K, Kemmler M, Turad M, Werner R, Kleisz E, Menzel S, Klingeler R, Büchner B, Kleiner R *et al.* 2010 *Superconductor Science and Technology* **24** 015015

[84] Arpaia R, Golubev D, Baghdadi R, Ciancio R, Dražić G, Orgiani P, Montemurro D, Bauch T and Lombardi F 2017 *Physical Review B* **96** 064525

[85] Savvides N and Katsaros A 1994 *Physica C: Superconductivity* **226** 23–36

[86] Cieplak M Z, Guha S, Vadlamannati S, Giebultowicz T and Lindenfeld P 1994 *Physical Review B* **50** 12876

[87] Matsuda Y, Komiyama S, Onogi T, Terashima T, Shimura K and Bando Y 1993 *Physical Review B* **48** 10498

[88] Hamalainen M, Hari R, Lounasmaa O V, Knuutila J and Ilmoniemi R J 1993 *Rev. Mod. Phys.* **65** 413–497

[89] Zotev V S, Matlashov A N, Volegov P L, Savukov I M, Espy M A, Mosher J C, Gomez J J and Kraus Jr R H 2008 *Journal of Magnetic Resonance* **194** 115–120

[90] Clarke J 1983 *IEEE Trans. Magn.* **19** 288–294

[91] Weinstock H 2012 *SQUID sensors: fundamentals, fabrication and applications* vol 329 (Springer Science & Business Media)

[92] Chi C, Santhanam P and Blöchl P 1992 *Journal of low temperature physics* **88** 163–195

[93] Van Duzer T and Turner C W 1981

[94] Clarke J and Braginski A I 2006 *The SQUID handbook: Applications of SQUIDs and SQUID systems* (John Wiley & Sons)

[95] Chwala A, Stolz R, IJsselsteijn R, Schultze V, Ukhansky N, Meyer H G and Schüler T 2001 *Superconductor Science and Technology* **14** 1111

[96] Faley M I, Maslennikov Y V, Koshelets V P and Dunin-Borkowski R E 2018 *IEEE Trans. Appl. Supercond.* **28** 1–5

[97] Chukharkin M, Kalabukhov A, Schneiderman J F, Öisjöen F, Jönsson M, Xie M, Snigirev O V and Winkler D 2013 *IEEE Trans. Appl. Supercond.* **23**

[98] Öisjöen F, Schneiderman J F, Figueras G, Chukharkin M, Kalabukhov A, Hedström A, Elam M

and Winkler D 2012 *Appl. Phys. Lett.* **100** 132601

[99] Tinchev S 1993 *IEEE transactions on applied superconductivity* **3** 28–32